

## Supporting Information

### Cu-In Halide Perovskite solar absorbers

Xin-Gang Zhao,<sup>†</sup> Dongwen Yang,<sup>†</sup> Yuanhui Sun,<sup>†</sup> Tianshu Li,<sup>†</sup> Lijun Zhang,<sup>\*,†</sup> Liping Yu,<sup>‡</sup> and Alex Zunger<sup>§</sup>

<sup>†</sup>State Key Laboratory of Superhard Materials, Key Laboratory of Automobile Materials of MOE, and College of Materials Science and Engineering, Jilin University, Changchun 130012, China

<sup>‡</sup>Department of Physics, Temple University, Philadelphia, PA 19122, United States

<sup>§</sup>University of Colorado, Renewable and Sustainable Energy Institute, Boulder, Colorado 80309, United States

#### Corresponding Author

\* [lijun\\_zhang@jlu.edu.cn](mailto:lijun_zhang@jlu.edu.cn)

# I. Detailed Computational Procedures

*Structure optimization:* All the candidate  $A_2[BC]X_6$  CIHPs in the cubic double-perovskite  $Fm\bar{3}m$  structure are optimized theoretically via total energy minimization with the conjugate-gradient algorithm. Both lattice parameters and internal atomic coordinates are fully relaxed. We used the high enough kinetic energy cutoffs for the plane-wave basis sets, *i.e.*, K/Rb/Cs: 337/286/286 eV; Cu/Ag: 355/325 eV; Ga/In: 175/125 eV; Cl/Br/I: 364/281/228 eV, to eliminate the potential Pulay stress error during crystalline cell optimization. The  $k$ -points meshes with grid spacing of less than  $2\pi \times 0.10 \text{ \AA}^{-1}$  are used for electronic Brillouin zone integration. The convergence threshold for the residual forces on atoms is set to 0.0002 eV/ $\text{\AA}$ .

*Band Gap:* As known, DFT calculations usually seriously underestimate (by ~50-100%) the band gaps of most of semiconducting materials. To remedy this problem, we employ the Heyd-Scuseria-Ernzerhof (HSE) hybrid functional approach<sup>1</sup> to reduce the self-interaction error and approach real gap values. The standard 25% exact Fock exchange is included. The HSE functional is used both for structural optimization and for evaluating the band gap at the optimized geometry. After obtaining the reliable HSE band gaps, the band structure, density of states, and absorption spectrum from the DFT-PBE calculations are corrected by the scissor operator to match the HSE gap values.

*Phase stability diagram analysis:* To guarantee a stable  $A_2[BC]X_6$  CIHP in materials growth, thermodynamic equilibrium condition requires that the following three relations need to be satisfied.<sup>2,3</sup>

$$2\Delta\mu_A + \Delta\mu_B + \Delta\mu_C + 6\Delta\mu_X = \Delta H_f(A_2BCX_6), \quad (1)$$

$$\Delta\mu_i \leq 0 (i = A, B, C, X), \quad (2)$$

$$h_j\Delta\mu_A + k_j\Delta\mu_B + n_j\Delta\mu_C + m_j\Delta\mu_X \leq \Delta H_f(A_{n_j}B_{k_j}C_{n_j}X_{m_j}), j = 1 \cdots Z, \quad (3)$$

where  $\Delta\mu_i = \mu_i - \mu_i^0$  is deviation of the chemical potential of atomic specie  $i$  during growth ( $\mu_i$ ) from that of its solidified or gas phase ( $\mu_i^0$ ),  $\Delta H_f$  is heat of formation, and  $A_{n_j}B_{k_j}C_{n_j}X_{m_j}$  represents all the existing competing phases (with the total number of  $Z$ ). Eq. (1) is for thermodynamic equilibrium, eq. (2) is to prevent atomic species from precipitating to elemental phases, and eq. (3) is to avoid formation of any secondary competing phase. Eq. (1) determines only three  $\Delta\mu_i$  are independent. Solutions to this group of equations, *i.e.*, the ranges of  $\Delta\mu_i$  that stabilize the  $A_2[BC]X_6$  CIHP, are bound in a polyhedron in the three-dimensional space with three  $\Delta\mu_i$  as variables. The 2-dimensional slices of the 3-dimensional stable polyhedron region taken at selected constant  $\Delta\mu_i$  for the thermodynamically stable CIHP compounds are shown in Supplementary Figure S4-S9. The corresponding four-element phase diagrams of A-B-C-X system are depicted in Supplementary Figure S11.

*Phonon spectrum:* To evaluate dynamical phonon stability, we calculate harmonic phonon spectrum (at 0 K) and room-temperature (300 K) phonon spectrum with inclusion of phonon-phonon interactions (anharmonic effects). The harmonic phonon spectrum is calculated from second-order interatomic force constants obtained by using the real-space finite-difference approach implemented in Phonopy code.<sup>4</sup> The  $2 \times 2 \times 2$  supercell (of the primitive cell of the double-perovskite structure) accompanying with the  $k$ -point mesh with grid spacing of  $2\pi \times 0.03 \text{ \AA}^{-1}$  is used for these

calculations. The room-temperature phonon spectrum is obtained by taking into account anharmonic phonon-phonon interaction with a self-consistent *ab initio* lattice dynamical (SCAILD) method.<sup>5</sup> This is done via calculating the phonon frequencies renormalization induced by phonon entropy, *i.e.*, the geometric disorder introduced by several frozen phonons simultaneously presenting in the simulated supercell. The SCAILD method alternates between creating atomic displacements in terms of phonon modes and evaluating phonon frequencies from calculated forces acting on the displaced atoms. The self-consistent cycle was terminated when the difference in the system free energy between two consecutive iterations is less than 1 meV. Calculations are performed at constant volume with thermal expansion effect ignored.

*Absorption spectrum:* The photon energy ( $\omega$ ) dependent absorption coefficient  $\alpha(\omega)$  is calculated from real/imaginary parts of dielectric function [ $\epsilon_1(\omega)/\epsilon_2(\omega)$ ]. The  $\epsilon_2(\omega)$  is calculated in the random phase approximation,<sup>6</sup> and  $\epsilon_1(\omega)$  is evaluated from  $\epsilon_2(\omega)$  via the Kramers-Kronig relation. The dense  $k$ -point meshes with grid spacing of less than  $2\pi \times 0.015 \text{ \AA}^{-1}$  is used for calculating ground-state band structure to guarantee  $\epsilon_2(\omega)$  converged. The twice of the number of occupied valence bands is used for calculating empty conduction band states.

*Maximum solar cell efficiency:* The maximum solar cell efficiency is simulated through calculating spectroscopic limited maximum efficiency (SLME) based on the improved Shockley-Queisser model. The detailed calculation procedure was described elsewhere.<sup>7,8</sup> It takes into account the effects of key intrinsic materials properties such as band gap, shape of absorption spectra, and material-dependent nonradiative recombination losses, on the photovoltaic efficiency. The simulation is performed under the standard AM1.5G solar spectrum at room temperature.

## II. Goldschmidt's empirical rule on formability of halide perovskites

To approximately assess structural stability of candidate CIHPs from point of view of ions close packing, we calculate the Goldschmidt tolerance factor  $t$  and the octahedral factor  $\mu$  within the framework of idealized solid-sphere model. The statistically established empirical criteria for formability of halide perovskites is  $0.81 < t < 1.11$  and  $0.44 < \mu < 0.90$ .<sup>9</sup> For the current quaternary  $A_2[BC]X_6$  double-perovskite system the effective  $t$  and  $\mu$  are defined as  $t_{eff} = (R_A + R_X) / \sqrt{2}((R_B + R_C) / 2 + R_X)$  and  $\mu_{eff} = (R_B + R_C) / 2R_X$ , where  $R$  are Shannon ionic radii<sup>10</sup> and the average between  $R_B$  and  $R_C$  are taken as the effective radius of the octahedral-site ion. The results are summarized in Supplementary Figure S12. The values of  $t_{eff}$  lie in the range of 0.86~1.04, all satisfying the stable criterion of  $t$ . Turning to  $\mu_{eff}$ , we find less than half of candidate CIHPs meet the stable criterion and generally the compounds with positive  $\Delta H_{dec}$  (see text) have the higher  $\mu_{eff}$  (falling in or approaching the stable region).

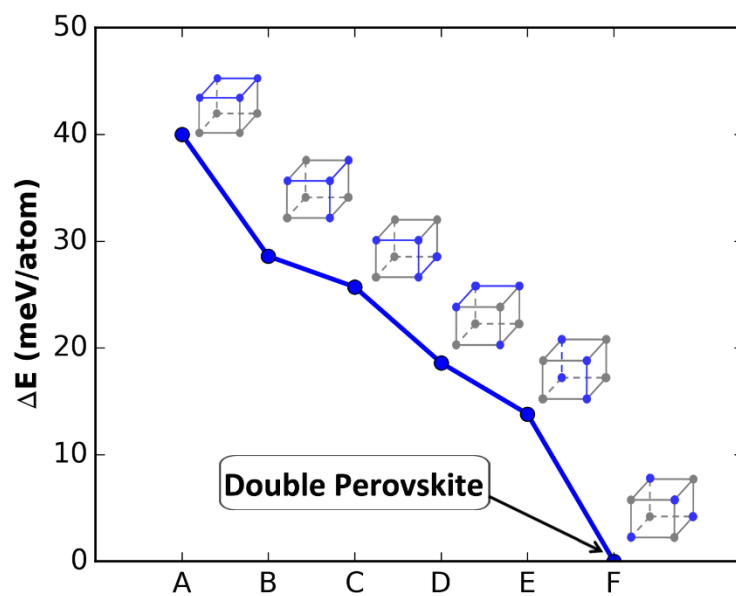


**Figure S1.** Energies of  $\text{Cs}_2\text{AgInCl}_6$  composed of different types of  $\text{AgCl}_6$  (in grey) +  $\text{InCl}_6$  (in blue) motifs arrangements. The calculations are performed with  $2 \times 2 \times 2$  supercell of standard cubic perovskite structure. The total number of structural configurations is 6. The lowest-energy configuration **F** (set to energy zero) corresponds to the double-perovskite or elpasolite structure (in space group of  $Fm\bar{3}m$ ), where the  $\text{AgCl}_6$  and  $\text{InCl}_6$  motifs alternate along the three crystallographic axes, forming the rock-salt type ordering.

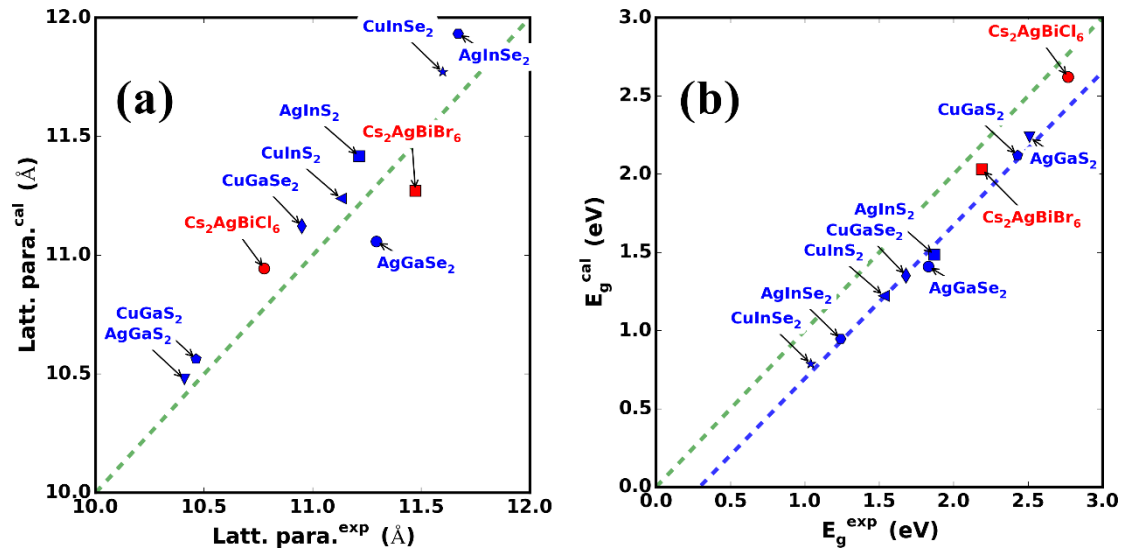


**Figure S2.** Calculated lattice parameters (a) and band gaps (b) for known chalcopyrites and Bi-based  $A_2[BC]X_6$  halide perovskites, compared with experimental data. Lattice parameter  $c$  is taken for tetrahedral chalcopyrites. The HSE functional is used both for structural optimization and for evaluating the band gap at the optimized geometry. The experimental data are taken from Ref. 11 for chalcopyrites and Ref. 12 for Bi-based halide perovskites.

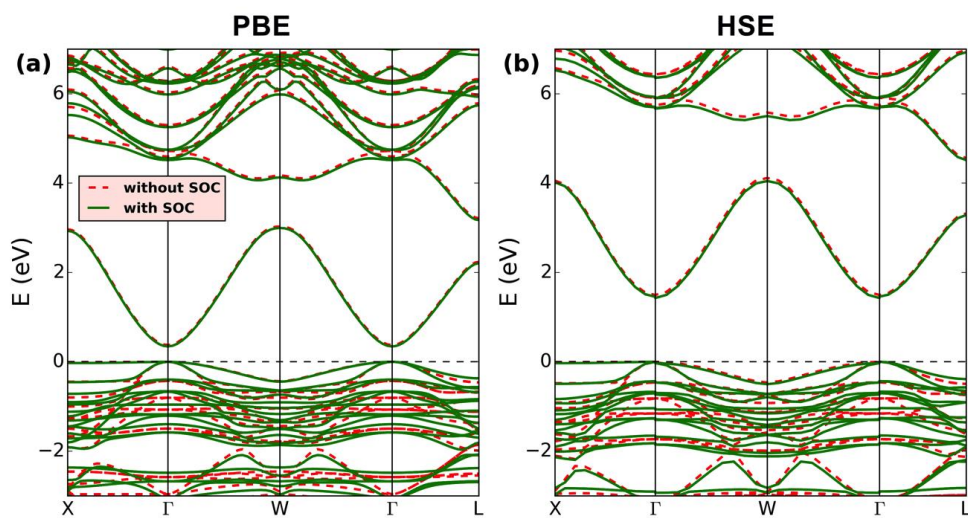


**Figure S3.** Effect of spin-orbit coupling (SOC) on band structure of  $\text{Cs}_2\text{AgInBr}_6$ . The results with/without inclusion of the SOC are shown by solid green/dash red lines. For both cases the valence band maximum is set to energy zero. Examination is carried out by using both the (a) PBE and (b) HSE functionals. One sees that the SOC has mild effect on the band structure of the CIHP compounds.

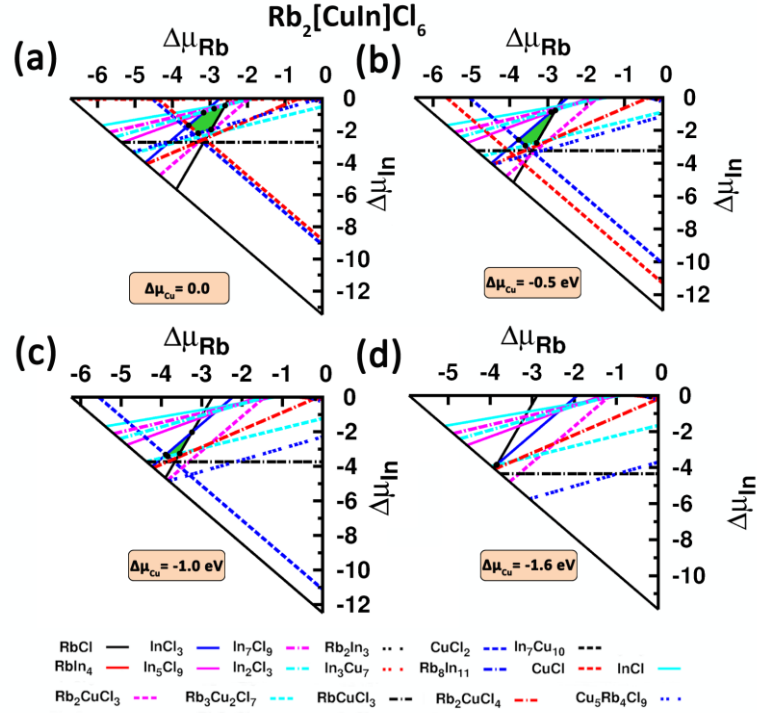


**Figure S4.** The phase stability diagram analysis (as described in Supplementary Sec. I) results sliced at several Cu-varied growth conditions represented by  $\Delta\mu_{\text{Cu}}$  (see text) for  $\text{Rb}_2[\text{CuIn}]\text{Cl}_6$ . The polygon region in green represents thermodynamic stable condition and each line corresponds to one competing phase. The main directly competing phases, which critically control the CIHP compound stability and correspond to the lines surrounding the green stable polygon region, are  $\text{InCl}_3$ ,  $\text{RbCl}$ ,  $\text{CuCl}_2$ ,  $\text{In}_2\text{Cl}_3$ ,  $\text{CuCl}$ ,  $\text{Rb}_3\text{Cu}_2\text{Cl}_7$ , and  $\text{Rb}_4\text{Cu}_5\text{Cl}_9$ . The last subplot (d) represents the critical condition of the thermodynamic stability, at which the green stable polygon region shrinks to a point and is disappearing.

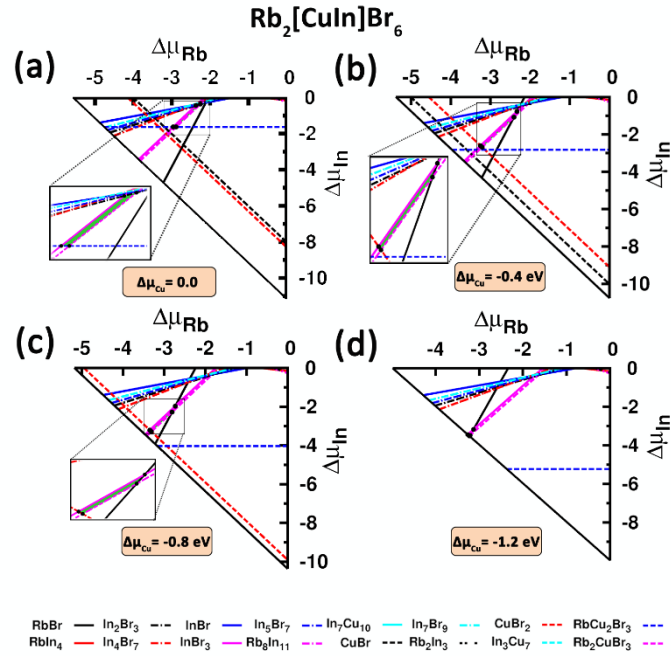


**Figure S5.** The phase stability diagram analysis results sliced at several Cu-varied growth conditions represented by  $\Delta\mu_{\text{Cu}}$  (see text) for  $\text{Rb}_2[\text{CuIn}]\text{Br}_6$ . The polygon region in green represents thermodynamic stable condition and each line corresponds to one competing phase. The main directly competing phases, which critically control the CIHP compound stability and correspond to the lines surrounding the green stable polygon region, are  $\text{RbIn}_4$ ,  $\text{InBr}_3$ ,  $\text{Rb}_2\text{CuBr}_3$ , and  $\text{RbBr}$ . The last subplot (d) represents the critical condition of the thermodynamic stability, at which the green stable polygon region shrinks to a point and is disappearing.

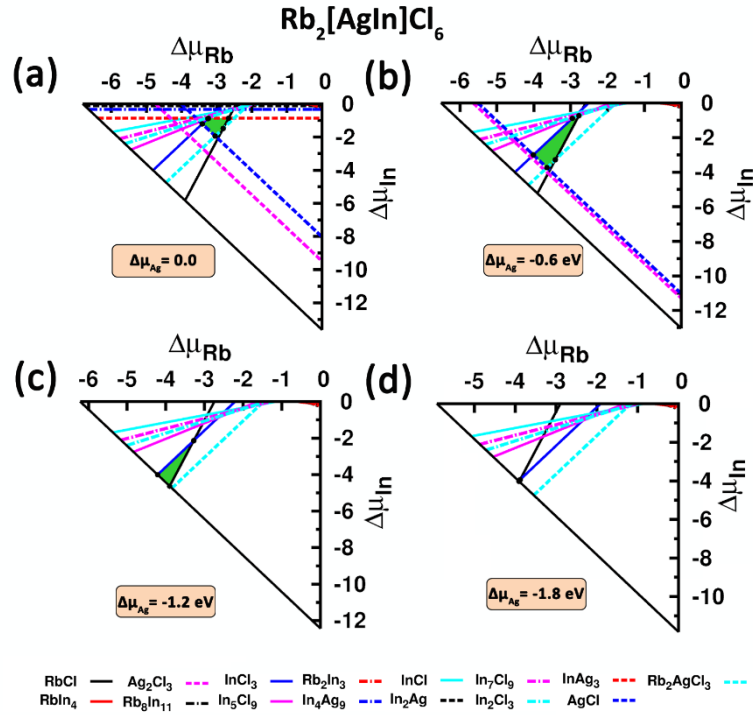


**Figure S6.** The phase stability diagram analysis results sliced at several Ag-varied growth conditions represented by  $\Delta\mu_{Ag}$  (see text) for Rb<sub>2</sub>[AgIn]Cl<sub>6</sub>. The polygon region in green represents thermodynamic stable condition and each line corresponds to one competing phase. The main directly competing phases, which critically control the CIHP compound stability and correspond to the lines surrounding the green stable polygon region, are InCl<sub>3</sub>, RbCl, AgCl, InAg<sub>3</sub>, and In<sub>2</sub>Cl<sub>3</sub>. The last subplot (d) represents the critical condition of the thermodynamic stability, at which the green stable polygon region shrinks to a point and is disappearing.

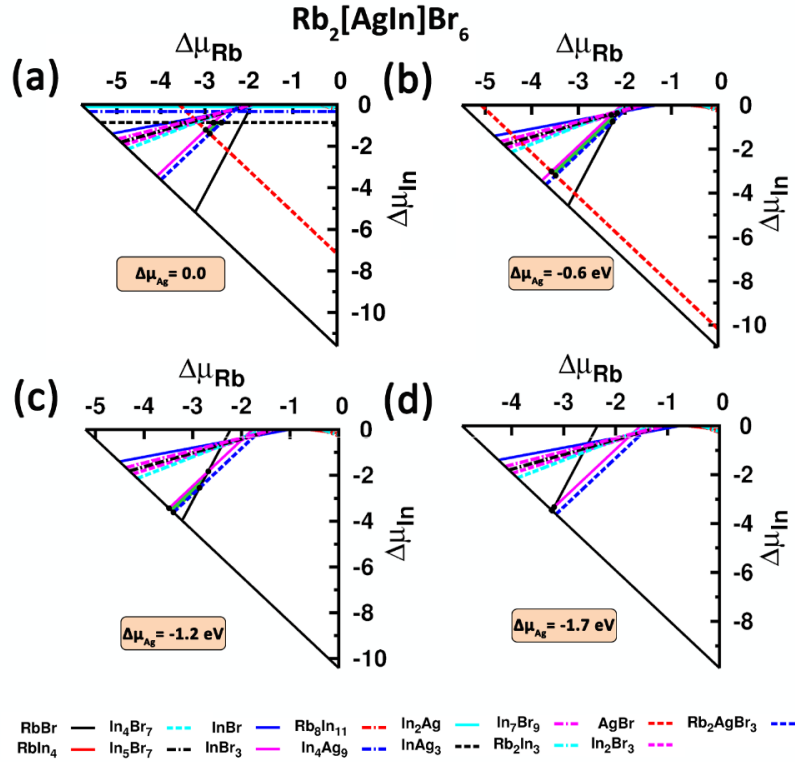


**Figure S7.** The phase stability diagram analysis results sliced at several Ag-varied growth conditions represented by  $\Delta\mu_{\text{Ag}}$  (see text) for  $\text{Rb}_2[\text{AgIn}]\text{Br}_6$ . The polygon region in green represents thermodynamic stable condition and each line corresponds to one competing phase. The main directly competing phases, which critically control the CIHP compound stability and correspond to the lines surrounding the green stable polygon region, are  $\text{InBr}_3$ ,  $\text{RbBr}$ ,  $\text{Rb}_2\text{AgBr}_3$ ,  $\text{AgBr}$ , and  $\text{InAg}_3$ . The last subplot (d) represents the critical condition of the thermodynamic stability, at which the green stable polygon region shrinks to a point and is disappearing.

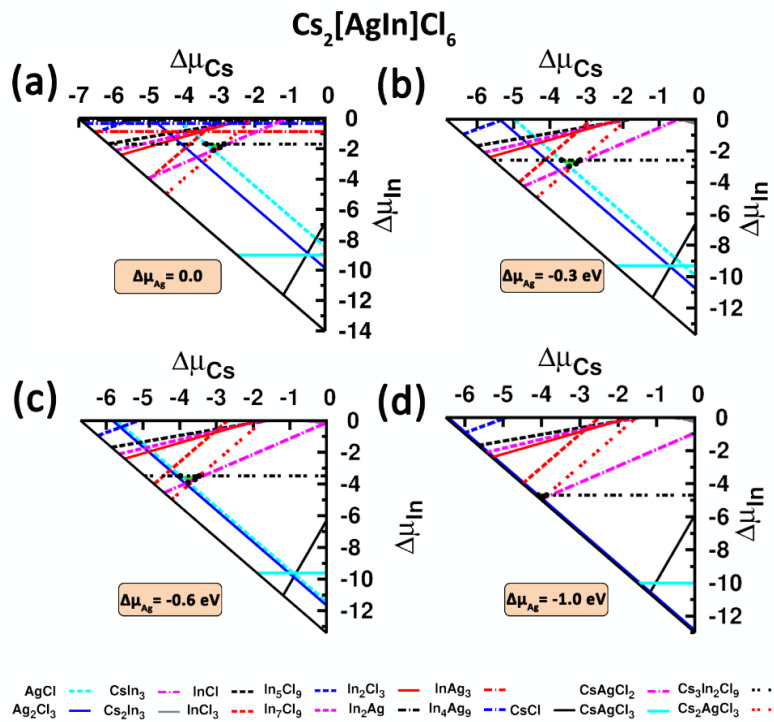


**Figure S8.** The phase stability diagram analysis results sliced at several Ag-varied growth conditions represented by  $\Delta\mu_{\text{Ag}}$  (see text) for Cs<sub>2</sub>[AgIn]Cl<sub>6</sub>. The polygon region in green represents thermodynamic stable condition and each line corresponds to one competing phase. The main directly competing phases, which critically control the CIHP compound stability and correspond to the lines surrounding the green stable polygon region, are Cs<sub>3</sub>In<sub>2</sub>Cl<sub>9</sub>, AgCl, CsAgCl<sub>2</sub>, and Cs<sub>2</sub>AgCl<sub>3</sub>. The last subplot (d) represents the critical condition of the thermodynamic stability, at which the green stable polygon region shrinks to a point and is disappearing.

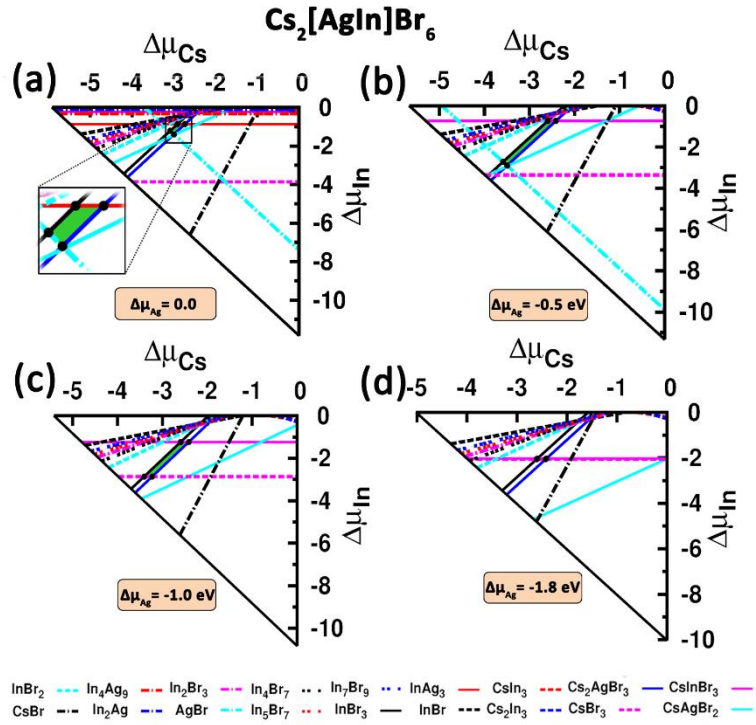


**Figure S9.** The phase stability diagram analysis results sliced at several Ag-varied growth conditions represented by  $\Delta\mu_{\text{Ag}}$  (see text) for Cs<sub>2</sub>[AgIn]Br<sub>6</sub>. The polygon region in green represents thermodynamic stable condition and each line corresponds to one competing phase. The main directly competing phases, which critically control the CIHP compound stability and correspond to the lines surrounding the green stable polygon region, are InBr<sub>3</sub>, Cs<sub>2</sub>AgBr<sub>3</sub>, InAg<sub>3</sub>, AgBr, CsAgBr<sub>2</sub>, and CsInBr<sub>3</sub>. The last subplot (d) represents the critical condition of the thermodynamic stability, at which the green stable polygon region shrinks to a point and is disappearing.

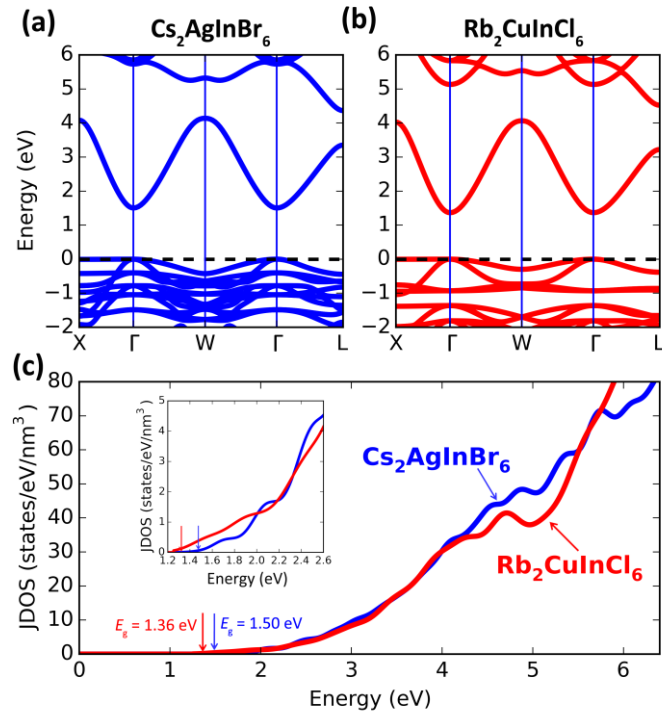


**Figure S10.** Calculated electronic band structures (a, b) and (c) joint density of states (JDOS) of  $\text{Cs}_2\text{AgInBr}_6$  and  $\text{Rb}_2\text{CuInCl}_6$ . In (a, b) the valence band maximum is set to energy zero. The inset of (c) shows the zoomed-in plot of JDOS in proximity to the band gap.

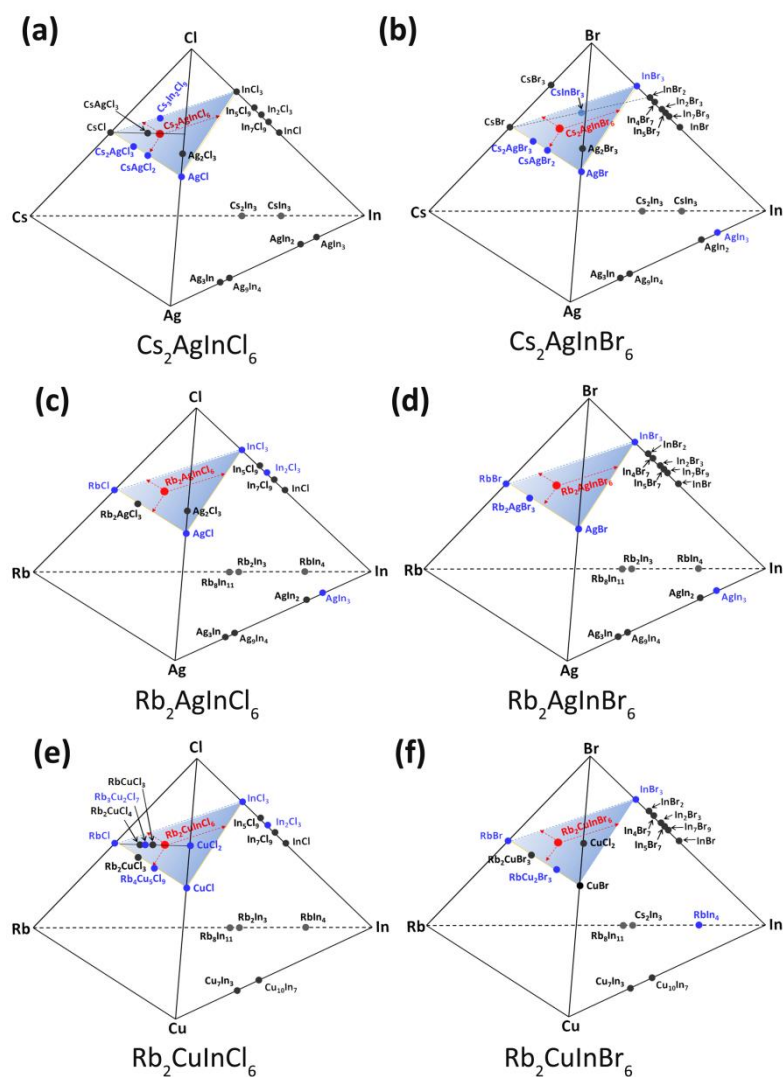


**Figure S11.** Tetrahedral phase diagram of quaternary A-B-C-X system for the six proposed optimal CIHP A<sub>2</sub>BCX<sub>6</sub> compounds. All the known existing (binary and ternary) phases (considered by the phase stability diagram analysis in Figure 3 of the main text and Supplementary Figure S4-S9) are mapped into the tetrahedron with elemental compositions of A, B, C, and X as vertexes. The directly competing phases, which critically control the CIHP compound stability and correspond to the lines surrounding the green stable polygon region in Figure 3, are shown in blue.

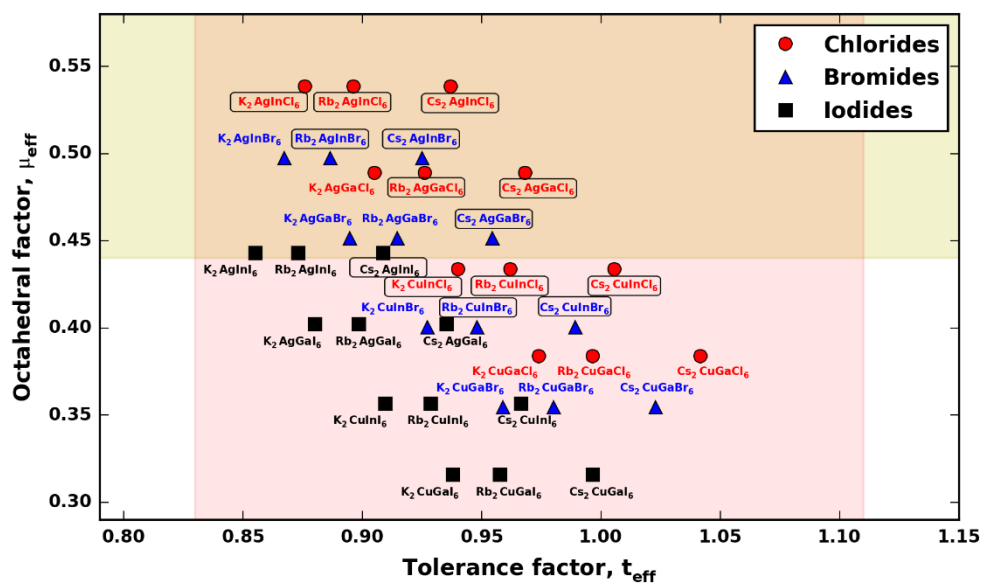


**Figure S12.** Mapping of all the candidate CIHPs onto two-dimensional plot with the effective Goldschmidt tolerance factor  $t_{\text{eff}}$  and the effective octahedral factor  $\mu_{\text{eff}}$  as variables. The statistically established empirical criteria for formability of halide perovskites,<sup>[9]</sup> *i.e.*,  $0.81 < t < 1.11$  and  $0.44 < \mu < 0.90$ , is shaded. Formulas of the CIHPs with positive decomposition enthalpy ( $\Delta H_{\text{dec}}$ , see Table S1) are marked in rounded squares.

**Table S1.** Calculated explicit data of lattice parameter ( $a$ ), band gap ( $E_g$ ), decomposition enthalpy with respect to the disproportionation channel into binary competing phases ( $\Delta H_{\text{dec}}$ ), thermodynamically stable condition (with respect to the disproportionation channels into all possible competing phases, see Supplementary Sec. I), carrier effective masses ( $m_e^*$  for electron,  $m_{lh}^*$  for heavy hole, and  $m_{hh}^*$  for light hole), and exciton binding energy ( $E_b$ , evaluated by using the hydrogen-like Wannier-Mott exciton model) for 36 candidate CIHPs considered for materials screening. The  $E_g$  is calculated by using the HSE functional with standard 25% exact Fock exchange. The effective masses and  $E_b$  are calculated only for six thermodynamically stable CIHPs. For the  $E_b$ , two values are calculated by using  $m_{lh}^*$  (the former) and  $m_{hh}^*$  (the latter), respectively.

$A_2BCX_6$				$a$ (Å)	$E_g$ (eV)	$\Delta H_{\text{dec}}$ (meV/atom)	Stable? ( $\times/\sqrt$ )	$m^*$			$E_b$ (meV)
A	B	C	X					$m_e^*$ ( $m_0$ )	$m_{lh}^*$ ( $m_0$ )	$m_{hh}^*$ ( $m_0$ )	
Cs	Cu	Ga	Cl	10.107	1.43	-7	$\times$	--	--	--	--
	Cu	Ga	Br	10.660	0.50	-23	$\times$	--	--	--	--
	Cu	Ga	I	--	--	-74	--	--	--	--	--
	Cu	In	Cl	10.333	1.40	77	$\times$	--	--	--	--
	Cu	In	Br	10.883	0.67	23	$\times$	--	--	--	--
	Cu	In	I	--	--	-22	--	--	--	--	--
	Ag	Ga	Cl	10.369	2.56	40	$\times$	--	--	--	--
	Ag	Ga	Br	10.914	1.32	13	$\times$	--	--	--	--
	Ag	Ga	I	--	--	-51	--	--	--	--	--
	Ag	In	Cl	10.594	2.52	116	$\sqrt$	0.32	0.43	2.38	195/304
	Ag	In	Br	11.156	1.50	56	$\sqrt$	0.24	0.34	1.37	97/139
Ag	In	I	11.962	0.31	3	--	--	--	--	--	
K	Cu	Ga	Cl	9.848	1.30	-25	$\times$	--	--	--	--
	Cu	Ga	Br	10.462	0.41	-72	$\times$	--	--	--	--
	Cu	Ga	I	--	--	-133	--	--	--	--	--
	Cu	In	Cl	10.135	1.35	36	$\times$	--	--	--	--
	Cu	In	Br	10.724	0.62	-42	$\times$	--	--	--	--
	Cu	In	I	--	--	-91	--	--	--	--	--
	Ag	Ga	Cl	10.164	2.44	-7	$\times$	--	--	--	--
	Ag	Ga	Br	10.745	1.22	-55	$\times$	--	--	--	--
	Ag	Ga	I	--	--	-120	--	--	--	--	--
	Ag	In	Cl	10.464	2.48	51	$\times$	--	--	--	--
	Ag	In	Br	11.023	1.44	-25	$\times$	--	--	--	--
Ag	In	I	11.806	0.26	-75	--	--	--	--	--	
Rb	Cu	Ga	Cl	9.940	1.34	-5	$\times$	--	--	--	--
	Cu	Ga	Br	10.532	0.43	-25	$\times$	--	--	--	--
	Cu	Ga	I	--	--	-107	--	--	--	--	--
	Cu	In	Cl	10.237	1.36	65	$\sqrt$	0.30	0.63	3.40	123/191
	Cu	In	Br	10.808	0.63	11	$\sqrt$	0.18	0.32	1.75	81/122
	Cu	In	I	--	--	-60	--	--	--	--	--
	Ag	Ga	Cl	10.204	2.48	24	$\times$	--	--	--	--
	Ag	Ga	Br	10.781	1.26	-1	$\times$	--	--	--	--
	Ag	Ga	I	--	--	-89	--	--	--	--	--
	Ag	In	Cl	10.520	2.50	89	$\sqrt$	0.32	0.41	2.35	234/327
	Ag	In	Br	11.064	1.46	34	$\sqrt$	0.24	0.32	1.81	75/100
Ag	In	I	11.901	0.27	-40	--	--	--	--	--	

## References:

- (1) Heyd, J.; Scuseria, G. E.; Ernzerhof, M. *J. Chem. Phys.* **2003**, *118*, 8207–8215.
- (2) Persson, C.; Zhao, Y.-J.; Lany, S.; Zunger, A. *Phys. Rev. B* **2005**, *72*, 35211.
- (3) Li, Y.; Singh, D. J.; Du, M.-H.; Xu, Q.; Zhang, L.; Zheng, W.; Ma, Y. *J. Mater. Chem. C* **2016**, *4*, 4592–4599.
- (4) Togo, A.; Tanaka, I. *Scr. Mater.* **2015**, *108*, 1–5.
- (5) Souvatzis, P.; Eriksson, O.; Katsnelson, M. I.; Rudin, S. P. *Phys. Rev. Lett.* **2008**, *100*, 95901.
- (6) Gajdoš, M.; Hummer, K.; Kresse, G.; Furthmüller, J.; Bechstedt, F. *Phys. Rev. B* **2006**, *73*, 45112.
- (7) Yu, L.; Zunger, A. *Phys. Rev. Lett.* **2012**, *108*, 68701.
- (8) Yu, L.; Kokenyesi, R. S.; Keszler, D. A.; Zunger, A. *Adv. Energy Mater.* **2013**, *3*, 43–48.
- (9) Li, C.; Lu, X.; Ding, W.; Feng, L.; Gao, Y.; Guo, Z. *Acta Crystallogr. B* **2008**, *64*, 702–707.
- (10) Shannon, R. D. *Acta Crystallogr. Sect. A* **1976**, *32*, 751–767.
- (11) Jaffe, J. E.; Zunger, A. *Phys. Rev. B* **1984**, *29*, 1882–1906.
- (12) McClure, E. T.; Ball, M. R.; Windl, W.; Woodward, P. M. *Chem. Mater.* **2016**, *28*, 1348–1354.